Efficient Parahydrogen Induced ^{13}C Hyperpolarization on a Microfluidic Device

Sylwia J. Barker,[†,‡] Laurynas Dagys,[†,¶] Malcolm H. Levitt,[†] and Marcel Utz[*,†,‡]

†*School of Chemistry, University of Southampton, Southampton, SO17 1BJ, United Kingdom*

‡*Institute of Microstructure Technology, Karlsruhe Institute of Technology, Karlsruhe, 76131, Germany*

¶*Institute of Chemical Physics, Vilnius University, Vilnius, 01513, Lithuania*

E-mail: marcel.utz@kit.edu

Abstract

We show the direct production and detection of ^{13}C-hyperpolarized fumarate by parahydrogen-induced polarization (PHIP) in a microfluidic Lab-on-a-Chip (LoC) device and achieve 8.5% ^{13}C polarization. This is the first demonstration of ^{13}C-hyperpolarization of a metabolite by PHIP in a microfluidic device. LoC technology allows the culture of mammalian cells in a highly controlled environment, providing an important tool for the life sciences. In-situ preparation of hyperpolarized metabolites greatly enhances the ability to quantify metabolic processes in such systems by microfluidic NMR. PHIP of ^{1}H nuclei has been successfully implemented in microfluidic systems, with mass sensitivities in the range of pmol$\sqrt{\text{s}}$. However, metabolic NMR requires high-yield production of hyperpolarized metabolites with longer spin life times than is possible with ^{1}H. This can be achieved by transfer of the polarization onto ^{13}C nuclei, which exhibit much longer T_1 relaxation times. We report an improved microfluidic PHIP device, optimised using a finite element model, that enables the direct and efficient production of ^{13}C hyperpolarized fumarate.

Introduction

Lab-on-a-Chip (LoC) systems that can culture cells, cell aggregates, or tissues, are increasingly adopted as a research tool in the life sciences, especially in drug development.[1–3] While this is partly driven by the widely recognised need to reduce animal testing, LoC cultures allow the use of human cells and can therefore provide more relevant models of human disease. Microfluidic technology enables precise control over the cellular growth environment, and offers high throughput and a high degree of reproducibility. In this way, cellular processes and functions as well as their response to external stimuli such as drugs,[4] therapeutic targets,[5–7] toxins,[8,9] and oxygen or nutrient supply[10,11] can be studied systematically. Microfluidic NMR[12–14] allows non-invasive and real-time *operando* quantitative characterisation of metabolic[15–17] and chemical[18] processes in LoC devices. However, sensitivity is limited in these systems due to their small size. Hyperpolarization of the nuclear spins[19] could address this, but requires preparation of hyperpolarized species that can be metabolized by the cultured cells, with a life time of the spin order long enough to detect downstream metabolic products.

Hyperpolarized metabolites have great potential as contrast agents for magnetic resonance imaging (MRI) and magnetic resonance spectroscopic imaging (MRSI), providing real-time and quantitative information on active metabolic pathways in healthy and diseased tissues.[20,21] This approach has been used *in vivo* for metabolic profiling of tumours such glioma,[22,23] hepatocellular carcinoma, lymphoma,[24,25] pancreatic[26] and breast cancers.[27,28] In this modality, relatively large amounts (several g) of hyperpolarized material (most commonly pyruvate) are prepared and injected intravenously into the patient. Preparation relies on either dissolution dynamic nuclear polarization[29,30] or on low-field polarization transfer based on Parahydrogen-Induced Polarization (PHIP).[31,32] The batch mode of operation of these methods does not lend itself to LoC culture devices, where a steady supply of much smaller amounts of hyperpolarized metabolites is needed. In this case, preparation methods that operate continuously at flow rates compatible with microfluidic systems (up to a few μl/min) are required.[33]

However, as the lifetime of hyperpolarized species is limited by nuclear relaxation, it is crucial

to produce them directly on the microfluidic device, in immediate proximity of their usage.

PHIP makes it possible to enhance NMR signals by up to 5 orders of magnitude.[34,35] It utilises *para*-hydrogen (p-H_2), the singlet nuclear spin isomer of molecular hydrogen, as a source of spin order. The nuclear spin order is transferred to a target molecule via a chemical reaction of p-H_2 with an unsaturated molecule in the presence of an organometallic catalyst. The chemical reaction is followed by spin manipulations to transfer the parahydrogen-derived spin order to a desired nucleus, and may include purification steps to remove unwanted compounds.[36]

LoC devices can be used to implement some or all of these processes. Eills et al. have reported mass sensitives of the order of pmol/s for ^{1}H in a microfluidic PHIP device[37] based on diffusion of p-H_2 through a silicone membrane, using propargyl acetate in methanol as a substrate. Barker et al. have subsequently shown that the same design can be used to directly hydrogenate acetylene dicarboxylic acid to produce ^{1}H-hyperpolarized fumarate.[38] However, the yield obtained in both cases falls short of the requirements for biological applications, particularly since further transformations such as purification and cleavage are required to effectively utilise the hyperpolarized material. To understand the interplay of the chemical, spatial and spin dynamics occurring on the microfluidic device proposed by Eills *et al.* Ostrowska *et al.*[39] developed a finite element model of reaction and found that insufficient uptake of hydrogen was the limiting factor of the reaction.

In the present contribution, we report an improved device design, optimised using this finite element model to maximise hydrogen uptake. Additionally, we introduce a variable temperature control to regulate the temperature at the sample detection chamber. It is shown that these improvements, taken together, increase the yield to such a point that the production and detection of ^{13}C-hyperpolarized fumarate becomes possible. To the best of our knowledge, this is the first report of PHIP-based ^{13}C hyperpolarization in a microfluidic system.

Materials and Methods

Microfluidic Set Up

The microfluidic device was manufactured from polycarbonate (PC) (Self Adhesive Supplies, UK) following the protocol given in Ref.[38] Briefly, devices were cut out with a LS3040 CO_2 laser cutter (HPC Laser, United Kingdom) from three layers of polycarbonate sheet material with 0.25, 0.5, and 0.25 mm thickness for the top, middle, and bottom layers, respectively. The sample chamber and channels were cut through the top layer and engraved in the middle and bottom layers. After plasma activating using Corona Treater (Electro-Technic Products, USA), each layer was coated with 18 μL of plasticiser (5 v/v% dibuthyl phtalate in isopropyl alcohol). Then the layers were dried for 15 mins at 65°C, assembled and bonded together under pressure and heat (5 tonnes, 85°C).

The microfluidic assembly consisted of the chip interposed between two 1 mm PDMS membranes (Shielding Solutions, UK) held together by a fluidic interface (ProtoLabs, UK). Connectors for 1/16" fluid and gas lines (Cole Parmer, UK) facilitated the delivery of substrates onto the chip shown in Fig 1. PDMS membranes that covered the upper part of the chip served a dual purpose. Firstly they promoted diffusion of hydrogen into the liquid channel and secondly, they enabled sealing of the assembly.

All experiments were conducted on a Bruker AVANCE III spectrometer operating at 11.7 T magnetic field. The microfluidic assembly was placed inside of a stripline-based micro-NMR probe for detection[40] as shown in Fig 1. The probe was equipped with hydrothermal sleeves that housed a thermistor regulated by temperature controller, allowing efficient heating of the sample detection chamber only. The calibration of the heater was recorded by Rogers *et al.* and shows temperature fluctuations of less than 0.1°C.[16]

The precursor solution was delivered into the chip using a syringe pump (Cole-Parmer, United Kingdom) located outside of the NMR spectrometer as illustrated in Fig. 1. Hydrogen gas (gas purity 99.995%) was delivered from a cyliner located outside of the spectrometer at a flow rate set

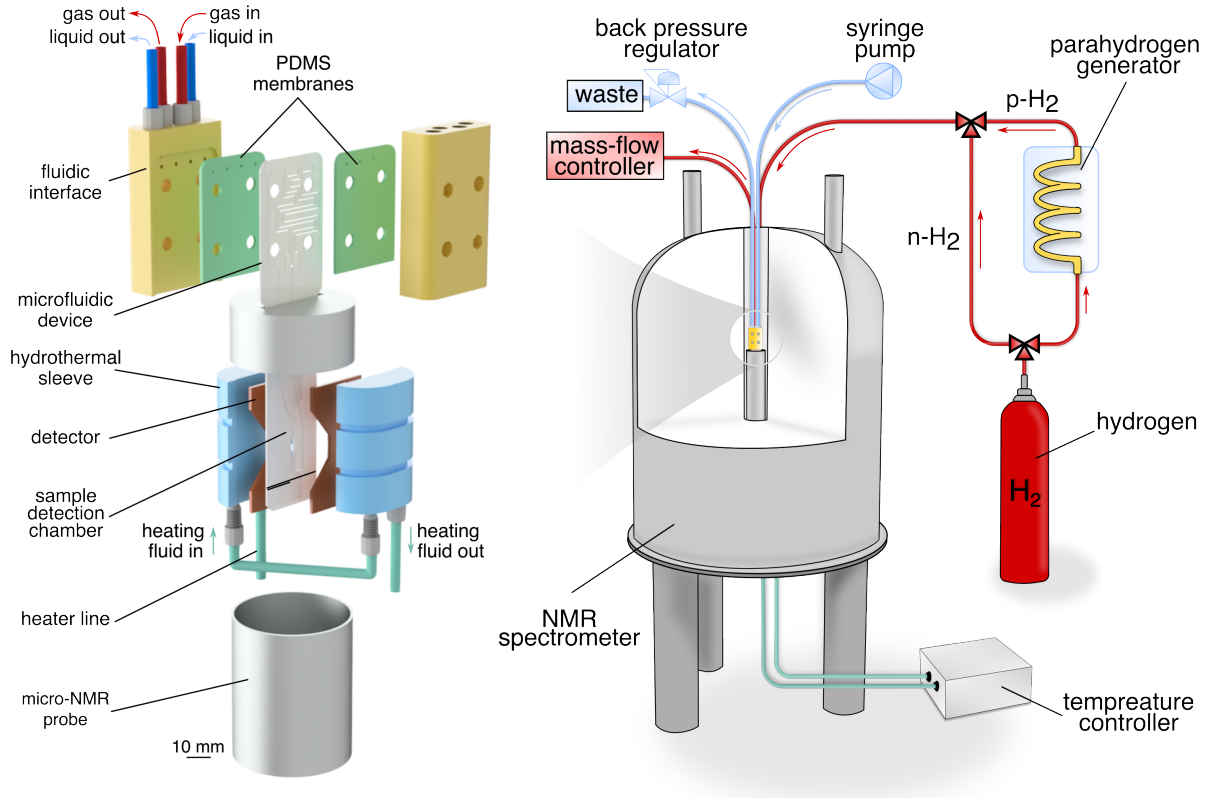

Figure 1: Experimental set up. The microfluidic chip assembly consists of a microfluidic device interposed between two PDMS membranes. These are held together by the fluidic interface that enables delivery of substrates into the chip. All experiments were performed inside of a high-field NMR spectrometer. Hydrogen/parahydrogen gas was supplied from a gas cylinder, while the precursor solution was introduced into the device using a syringe pump located outside of the spectrometer. The device was placed into the micro-NMR probe for detection. The probe was also equipped with hydrothermal sleeves regulated by temperature controller that enabled efficient heating of the sample detection chamber.

to 20 mL min^{-1} controlled using a mass-flow controller at the end of the gas line. The gas line was equipped with a valve selecting a flow of either hydrogen in thermal equilibrium or parahydrogen. Parahydrogen gas was obtained with 50% enrichment using a home-built parahydrogen generator filled with iron (III) oxide and cooled to 77 K.

All chemicals were purchased from Merck KGaA (Germany) and were used as received.

Quantification of Hydrogen Uptake into β-chip

The uptake of hydrogen into the β-chip was quantified by flowing a solution of 20 mM sodium acetate dissolved in methanol-d_4. In the gas channel, hydrogen in thermal equilibrium was supplied at 5 bar. The flow rate of hydrogen was controlled using a flow meter positioned at the end of the gas line, set to a constant rate of 20 mL min^{-1}. The flow rate of the liquid was varied from 2 to 20 μL min^{-1} in steps of 2 μL min^{-1} and the solution was left to equilibrate for 10 minutes at each flow rate. Then, 64 scans were acquired after the application of a $\frac{\pi}{2}$ pulse with a recycle delay of 20 s. The NMR signal at 4.55 ppm was integrated to determine the H_2 concentration.

Finite Element Modelling

Finite element simulations were performed using COMSOL Multiphysics version 5.4. Fig. 3a and Fig. 3b show simulation domains for the $\alpha-$ and β-chips, respectively. The key functional components are: the fluid channel, the sample chamber and PDMS membranes. The total volume of the β-chip was calculated as 7 μL. The simulation protocol and detailed results are given in the SI.

Formation of ^{13}C Hyperpolarized Fumarate

The precursor solution contained 100 mM acetylene dicarboxylic acid [1-^{13}C] disodium salt, 6 mM $[RuCp^*(CH_3CN)_3]PF_6$ catalyst and 200 mM sodium sulfite dissolved in D_2O at 50°C. The heater temperature was set to 58°C. Flow rates from 2 to 16 μL min^{-1} in steps of 2 μL min^{-1} were studied. Parahydrogen pressure was set to 6 bar. The probe delivered nutation frequencies for ^{13}C RF pulses of 12.5 kHz. Spectra were collected with a 200 ppm spectral width, and 8 k data points were acquired. Proton singlet order in [1-^{13}C]fumarate was converted into the observable carbon magnetisation using the singlet-to-heteronuclear-magnetisation (S2hM) pulse sequence.[41] The maximum efficiency was achieved using the following parameters: $\tau = 15.7$ ms, $n_2 = 7$, $n_1 = 7$. The repetition delay was set to 60 s. The yield of fumarate was determined by comparing

the integral of the fumarate peak at 6.8 ppm to the catalyst Cp* peak at 2.35 ppm (spectrum shown in the SI) and accounting for the difference in the number of protons. To calculate the enhancement factor for carbon polarization, the SNR of in the hyperpolarized spectrum was compared with the SNR obtained form a spectrum of 1M D-glucose-1-^{13}C averaged over 32 scans.

Results and Discussion

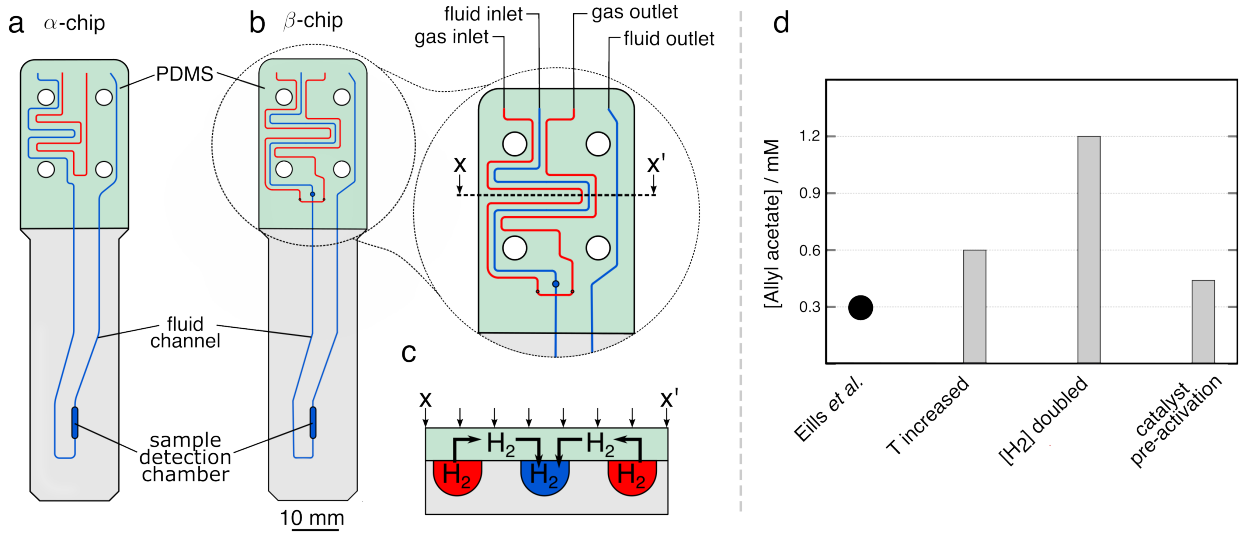

Figure 2: Top view of the microfluidic devices. a) The α-chip used by Eills *et al.*[37] Adapted from Ref.[39] Available under CC BY 4.0. Copyright Ostrowska *et al.*b) The β-chip. The key functional area of the β-chip was enlarged. c) Cross section of the β-chip. The PDMS membrane (green) acts as a bridge between the fluid (blue) and two gas (red) channels, enabling hydrogen to diffuse into the solution. d) Concentration of allyl acetate reported by Eills *et al.*[37] and three independent scenarios predicted by the model developed in Ref.[39]

The basic principle of operation of our PHIP device is shown schematically in Fig. 2. The solution containing an unsaturated precursor flows through the channel indicated in blue, next to a channel containing parahydrogen gas under pressure, shown in red. Both channels are covered by a PDMS membrane, through which the molecular hydrogen diffuses efficiently (Fig. 2c). Fig. 2 compares the original chip design used by Eills et al[42] (a) with an improved design used here (b). The length of the fluid path has been increased, and the fluid path is now flanked by the hydrogen gas channel on either side.

An FEM model of the transport and chemical kinetics of the para-hydrogenation of propargyl acetate to allyl acetate has been previously reported.[39] Fig. 2d shows the experimental yield of hyperpolarized allyl acetate reported by Eills *et al.*[37] along with the prediction of the FEM model, whose kinetic parameters have been obtained from independent experiments at large scale.[39] The model was used to explore three different hypothetical scenarios. In the first scenario all reaction rate constants were increased by a factor of two, approximating a temperature increase by about 10 °C. As shown in Fig. 2d, this leads to an increase in the yield by about a factor of two as expected. In the second case the partial pressure of hydrogen in the gas supply was doubled. The model predicts a massive increase in yield by a factor of four. Finally, the catalyst activation rate was increased 10 times, simulating a situation where the protection group of the catalyst was replaced with one that is easier to remove. This led only to a modest increase in the yield. From these findings, we concluded that improvement of the hydrogen uptake was the most efficient way of increasing the yield of hyperpolarized product.

Enhancing Hydrogen Uptake

Experiments by Eills et al. had been carried out with hydrogen gas at 5 bar. Simply elevating hydrogen pressure in the chip is not viable as it tends to cause delamination and leakages, and high hydrogen pressures pose a safety hazard. Instead, the channel network can be modified to maximise the gas uptake. The fluidic design in the α-chip used by Ellis *et al.* consisted of one gas and one fluid channel in a side-by-side arrangement, with a PDMS membrane covering both channels and serving as a diffusion conduit for H_2. The fluid channel in the β-chip design was positioned between two gas pathways, as shown in Fig. 3a and Fig. 3b. Additionally, the fluid pathway in contact with the PDMS membrane was extended by 30% in length. The finite element simulation domains for the $\alpha-$ and β-chips are shown in Fig. 3.

To experimentally measure the uptake of hydrogen gas into the β-chip, methanol was flowed into the fluid channel by means of a syringe pump located outside of the NMR spectrometer as shown in Fig. 1. The chip was pressurised to 5 bar with hydrogen gas and its flow was controlled

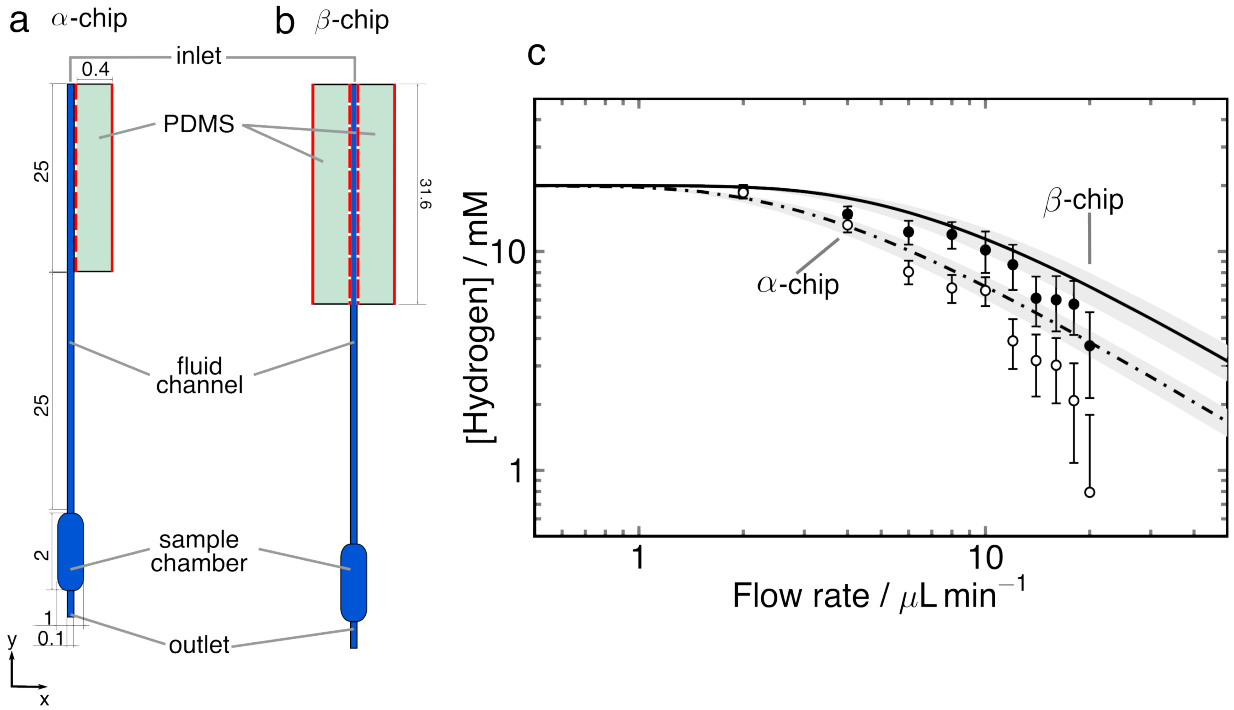

Figure 3: a) α-chip simulation domain. Adapted from Ref [39]. Available under CC BY 4.0. Copyright Ostrowska *et al.*b) β-chip simulation domain. c) Hydrogen uptake into the chip as a function flow rate. The solid empty and black circles represent the NMR data for $\alpha-$ and β-chips, respectively. The solid and dash-dotted lines are the results of FEM simulations. The grey shadows represent $\pm 1.5\,\mu$L error in the volume of the chip. Data for the α-chip was obtained from Eills *et al.* Ref. [37]

using a mass-flow controller set to 20 mL min^{-1}. Dissolved hydrogen was detected by NMR in the 2.5 μL sample chamber on the chip.

Fig. 3c shows the concentration of hydrogen in the sample chamber as a function of flow rate; 20 mM of sodium acetate was used as the concentration standard. The solid empty and black circles represent the NMR data for $\alpha-$ and β-chips, respectively. Error bars represent integrated rms noise in the spectra. Experimental NMR data for the α-chip was taken from Ref.[37] At 2 μL min^{-1} flow rate the flowing liquid in both devices is fully saturated with hydrogen. However, as the flow rate increases to 10 μL min^{-1}, the concentration of hydrogen in the β-chip is 11.3 mM versus only $\sim$6 mM in the α-chip. At a higher flow rate of 18 μL min^{-1} there is 3 times more hydrogen dissolved in the β-chip compared to the α-chip. The solid and dash-dotted lines are the FEM

simulations and the gray shadows represent uncertainty due to fabrication tolerances of the chips. Simulations for both the $\alpha-$ and the β-chip are in good agreement with the experimental data for flow rates up to 10 μL min^{-1}. Above this flow rate, the model consistently overestimates the hydrogen uptake. This discrepancy is not well understood yet, it was proposed that this could be due to the deformation of the PDMS membrane.[37] However, simulations and experiments both suggest that the hydrogen uptake of the β-chip is higher by a factor of two for flow rates above 2 $\mu L/$min.

The PHIP performance of the microfluidic chip was compared to the results obtained by Eills et al. To this effect, the precursor solution containing 20 mM of propargyl acetate and 5 mM of rhodium catalyst flowed in the solution channel, while 5 bar of *para*-enriched hydrogen gas was supplied into the gas channel. The experimental setup is shown schematically in Fig. 1. Hydrothermal sleeves were incorporated between the stripline detector and the microfluidic device housing, effectively heating the sample detection chamber. This facilitated efficient heating of the sample chamber up to 58°C. The experiments and results are described in detail in the SI. Briefly, at the optimal flow rate of 5μL min^{-1}, the concentration of allyl acetate at 25°C was determined to be 4.9 ± 0.2 mM, corresponding to a yield of $24.5 \pm 1\%$. Compared to the results reported by Eills et al, this represents an increase in yield by a factor of 15. Increasing the temperature to 37°C led to the concentration of allyl acetate of 7.0 ± 0.2 mM, corresponding to a yield of $35 \pm 1\%$. This represents a further 10% increase in yield compared to the initial conditions. Elevation of the temperature to 47°C led to a decrease in the concentration of allyl acetate to 5.4 ± 0.2 mM.

Formation of ^{13}C Hyperpolarized Fumarate

The short lifetime of ^{1}H polarization, of the order of seconds, limits application of ^{1}H-hyperpolarization to track metabolic processes. This can be overcome by transferring the polarization to a longer-lived nucleus such as ^{13}C or ^{15}N. Hyperpolarized fumarate is a promising target for *in vivo* detection of necrosis and therefore has been extensively used as a hyperpolarization target.[43–46] However, the trans-hydrogenation reaction to synthesise hyperpolarized fumarate is challenging

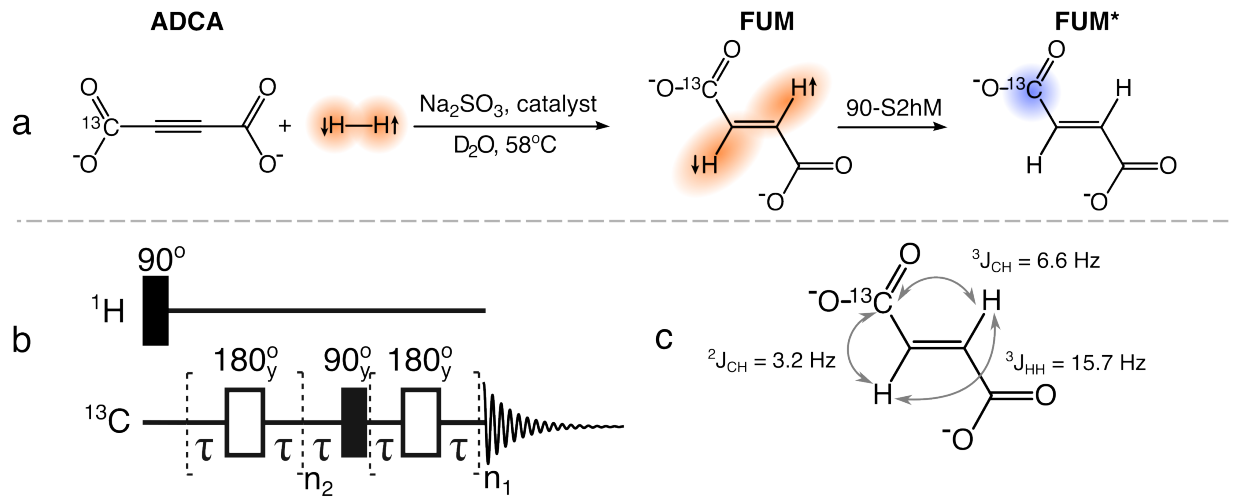

Figure 4: a) Formation of ^{13}C hyperpolarized fumarate. acetylene dicarboxylic acid [1-^{13}C] disodium salt labelled as molecule **ADCA** reacts with parahydrogen in the presence of sodium sulfite and the catalyst $[RuCp^*(CH_3CN)_3]PF_6$ in D_2O. The reaction results in a production of disodium [1-^{13}C]fumarate, molecule **FUM**, with the two protons in a singlet state. Application of the S2hM pulse sequence converts the singlet state into observable ^{13}Cmagnetisation **FUM***. b) 90-S2hM pulse sequence used to transfer the polarization from the proton singlet state to carbon. c) The $J-$coupling network of [1-^{13}C]fumarate. The $J-$coupling values were taken from Ref.[43]

as it is slow compared to the timeframe in which the hyperpolarization returns to thermal equilibrium.[47] As will be shown in the following, the enhanced hydrogen uptake of the β-chip together with the ability to run the reaction at slightly elevated temperature make it possible to hyperpolarize fumarate more efficiently.

As shown in Fig. 4a hyperpolarized fumarate was generated in aqueous solution via a reaction of $[1-^{13}$C]-acetylenedicarboxylic acid disodium salt (**ADCA**) with *para*$-$hydrogen in the presence of a ruthenium catalyst, resulting in $[1-^{13}$C]fumarate (**FUM**). Since the added protons are chemically and magnetically equivalent, a ^{13}C label is required to to break the symmetry and enable observation of the spin order by NMR. The pulse sequence to convert the resulting singlet spin order into ^{13}C magnetisation is shown in Fig. 4b . It consists of an initial purge pulse on the ^{1}H channel, followed by an S2hM sequence[41] on the ^{13}C channel. This hydrogenation reaction is known to be affected by singlet-triplet (S-T) mixing, which can lead to a reduction of observable PHIP signal.[48] S-T mixing occurs when molecules of hydrogen form intermediate hydride species

with the catalyst metal center. At high magnetic fields the two protons experience a chemical shift difference in the hydride, which can lead to significant leakage from the proton singlet state ($|S_0\rangle$) to the central triplet state ($|T_0\rangle$).[49] Partial signal cancellation occurs after S2M or S2hM sequences are applied which convert these states to either ^{1}H or ^{13}C magnetization but with opposite phases. There are methods for mitigating so-called S-T mixing.[48,50,51] A $\pi/2$ "purge" pulse prior to the S2M sequence was found to improve the efficiency of the sequence in microfluidic chips.[38] The purge pulse removes the detrimental population of the $|T_0\rangle$ state by transferring it to the two outer $|T_\pm\rangle$ states where it has no effect on the polarization transfer. Here, the purge pulse was applied on the ^{1}H channel prior to application of the S2hM sequence on the ^{13}C channel as shown in Fig. 4b.

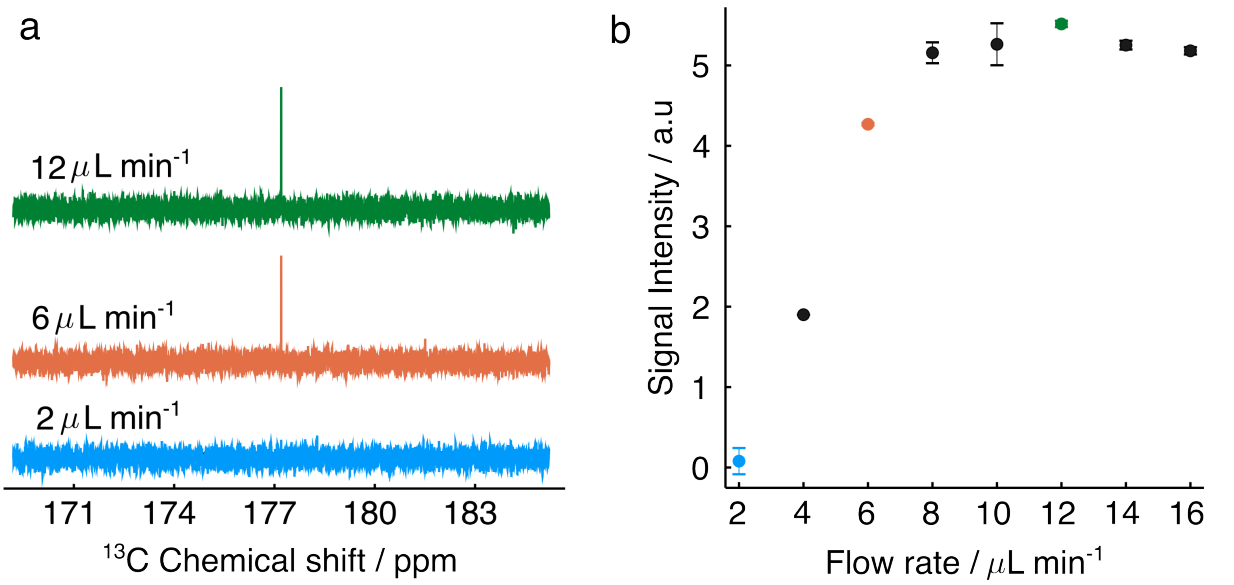

Figure 5: a) ^{13}C spectra of [1-^{13}C]fumarate at different flow rates. b) Hyperpolarized ^{13}C signal intensity of [1-^{13}C]fumarate as a function of fluid flow rate.

Fig. 5a shows single scan ^{13}C NMR spectra of ^{13}C-hyperpolarized fumarate obtained at different flow rates using the set-up depicted in Fig. 1 and the β-chip at a temperature of 58°C. At 2 μL min^{-1}, the carbon signal is barely distinguishable from the noise but as the flow rate increases, the signal intensity increases. The change in signal intensity as a function of flow rate is displayed in Fig. 5b. There is a gradual increase in signal intensity up to 8 μL min^{-1}, followed by a plateau. This behaviour is markedly different to what has been reported by Eills *et al.* for ^{1}H

hyperpolarization,[37] which exhibited a sharp maximum at the optimum flow rate. At very low flow rates the time it takes for the product to be delivered into the sample chamber is greater that the spin relaxation time. This seems to be the case at 2 μL min^{-1} and below. It should be noted that since the polarization transfer only takes place in the sample detection region, it is the ^{1}H singlet lifetime that is relevant here, not the ^{13}C T_1. Between 2 and 8 μL min^{-1} a gradually increasing amount of hyperpolarized material reaches the sample chamber. As shown in Fig. 3, the hydrogen uptake decreases rapidly with increasing flow rate. It appears that this effect, which must lead to a decreasing yield of hydrogenation product with increasing flow rate, is almost perfectly compensated by the shorter amount of time needed for the product to reach the detection chamber at flow rates between 8 and 16 μL min^{-1}. This gives rise to the hope that the ^{13}C polarization could be substantially improved if the polarization transfer step could be carried out further upstream in the chip. Further experiments and detailed simulations are needed to clarify this point in support of a corresponding redesign of the microfluidic setup.

A straightforward way to quantify the enhancement factor is to run the same experiment with hydrogen in thermal equilibrium. Unfortunately, the concentration of fumarate was too low for the thermal ^{13}C signal to be directly observed using our home-built transmission line probe, which is not optimised for sensitivity on the low frequency channel. To estimate the signal enhancement, the hyperpolarized spectrum was compared with a spectrum of 1M D-Glucose-1-^{13}C obtained after the application of $\frac{\pi}{2}$ pulse (see SI). The SNR in the glucose spectrum is 2:1, while in the hyperpolarized spectrum of fumarate the SNR is 9:1. Since the glucose spectrum was obtained with 32 scans, the SNR from a single scan is $\frac{2}{\sqrt{32}} \approx 0.35$. Accounting for the fact that glucose spectrum was obtained from a 1 M sample and the spectrum of fumarate was obtained from a 3 mM sample. This leads to the signal enhancement factor of $\varepsilon = \frac{9}{0.35} * \frac{1000}{3} \approx 8500$, corresponding to 8.5% ^{13}C polarization.

Conclusions

In this work we have used finite element simulation results to inform the design of an optimized microfluidic device for performing PHIP reactions. FEM of the chip reported by Ostrowska *et al.*[39] identified that inadequate uptake of hydrogen into the device is the limiting factor for the reaction, which resulted in sub-milimolar reaction yield. Introduction of an additional hydrogenation channel resulted in a 15-fold increase in the yield of hyperpolarized product compared with previously reported α-chip.[37] Heating the sample chamber of the chip led to a further improvement of the yield. With these improvements, it has become possible for the first time to demonstrate the production and observation of the ^{13}C hyperpolarized metabolite fumarate in a microfluidic device, with a ^{13}C polarization of 8.5%. Further improvements are possible by optimisation of the fluidic design, as well as by improvement of the ^{13}C sensitivity of the microfluidic NMR probe. The present results represent an important step towards the integrated production of hyperpolarized materials and microfluidic cell culture.[15,16] However, this requires integration of cleanup steps into the microfluidic system to remove the potentially toxic catalyst and reaction products. Research in this direction is underway in our laboratory, and will be reported at a later occasion.

Supporting Information Available

Supporting information includes data on allyl acetate pH$_2$ experiments, details on the FEM simulation model, the ^{1}H NMR spectrum of fumarate, as well as technical drawings of the microfluidic device. All raw experimental and simulation data has been deposited on zenodo.org, organised by Figure.[52]

Acknowledgments

The authors thank Dr. Manvendra Sharma for help with the design and setup of the microfluidic NMR probe and fluidic support systems. This work was supported by the UK Engineering

and Physical Sciences Research Council (EPSRC) through grants EP/W020343/1 paraQchip and EP/V055593/1, and the iCASE studentship EP/R513325/1 to SJB, co-funded by Bruker UK Ltd, as well as by the European Research Council grant 786707-FunMagResBeacons.

References

(1) Leung, C. M.; de Haan, P.; Ronaldson-Bouchard, K.; Kim, G.-A.; Ko, J.; Rho, H. S.; Chen, Z.; Habibovic, P.; Jeon, N. L.; Takayama, S.; Shuler, M. L.; Vunjak-Novakovic, G.; Frey, O.; Verpoorte, E.; Toh, Y.-C. A guide to the organ-on-a-chip. *Nat. Rev. Methods Primers* **2022**, *2*, 1–29.

(2) Ma, C.; Peng, Y.; Li, H.; Chen, W. Organ-on-a-Chip: A New Paradigm for Drug Development. *Trends Pharmacol. Sci.* **2021**, *42*, 119.

(3) Ingber, D. E. Human Organs-on-Chips for Disease Modelling, Drug Development and Personalized Medicine. *Nat. Rev. Genet.* **2022**, *23*, 467–491.

(4) Si, L.; Bai, H.; Rodas, M.; Cao, W.; Oh, C. Y.; Jiang, A.; Moller, R.; Hoagland, D.; Oishi, K.; Horiuchi, S.; Uhl, S.; Blanco-Melo, D.; Albrecht, R. A.; Liu, W.-C.; Jordan, T.; Nilsson-Payant, B. E.; Golynker, I.; Frere, J.; Logue, J.; Haupt, R.; McGrath, M.; Weston, S.; Zhang, T.; Plebani, R.; Soong, M.; Nurani, A.; Kim, S. M.; Zhu, D. Y.; Benam, K. H.; Goyal, G.; Gilpin, S. E.; Prantil-Baun, R.; Gygi, S. P.; Powers, R. K.; Carlson, K. E.; Frieman, M.; TenOever, B. R.; Ingber, D. E. A Human-Airway-on-a-Chip for the Rapid Identification of Candidate Antiviral Therapeutics and Prophylactics. *Nat. Biomed. Eng.* **2021**, *5*, 815–829.

(5) Wu, Q.; Liu, J.; Wang, X.; Feng, L.; Wu, J.; Zhu, X.; Wen, W.; Gong, X. Organ-on-a-chip: Recent Breakthroughs and Future Prospects. *Biomed. Eng. Online* **2020**, *19*, 1–19.

(6) Kolluri, N.; Klapperich, C. M.; Cabodi, M. Towards Lab-on-a-Chip Diagnostics for Malaria Elimination. *Lab Chip* **2017**, *18*, 75–94.

(7) Wu, J.; Dong, M.; Rigatto, C.; Liu, Y.; Lin, F. Lab-on-Chip Technology for Chronic Disease Diagnosis. *NPJ Digit. Med.* **2018**, *1*, 1–11.

(8) Jodat, Y. A.; Kang, M. G.; Kiaee, K.; Kim, G. J.; Martinez, A. F. H.; Rosenkranz, A.; Bae, H.; Shin, S. R. Human-Derived Organ-on-a-Chip for Personalized Drug Development. *Curr. Pharm. Des.* **2018**, *24*, 5471–5486.

(9) Cong, Y.; Han, X.; Wang, Y.; Chen, Z.; Lu, Y.; Liu, T.; Wu, Z.; Jin, Y.; Luo, Y.; Zhang, X. Drug Toxicity Evaluation Based on Organ-on-a-chip Technology: A Review. *Micromachines* **2020**, *11*, 381.

(10) Komen, J.; Westerbeek, E. Y.; Kolkman, R. W.; Roesthuis, J.; Lievens, C.; van den Berg, A.; van der Meer, A. D. Controlled Pharmacokinetic Anti-Cancer Drug Concentration Profiles Lead to Growth Inhibition of Colorectal Cancer Cells in a Microfluidic Device. *Lab Chip* **2020**, *20*, 3167–3178.

(11) Emami Nejad, A.; Najafgholian, S.; Rostami, A.; Sistani, A.; Shojaeifar, S.; Esparvarinha, M.; Nedaeinia, R.; Haghjooy Javanmard, S.; Taherian, M.; Ahmadlou, M.; Salehi, R.; Sadeghi, B.; Manian, M. The Role of Hypoxia in the Tumor Microenvironment and Development of Cancer Stem Cell: A Novel Approach to Developing Treatment. *Cancer Cell Int.* **2021**, *21*, 1–26.

(12) Badilita, V.; Meier, R. Ch.; Spengler, N.; Wallrabe, U.; Utz, M.; Korvink, J. G. Microscale Nuclear Magnetic Resonance: A Tool for Soft Matter Research. *Soft Matter* **2012**, *8*, 10583–10597.

(13) Finch, G.; Yilmaz, A.; Utz, M. An Optimised Detector for In-Situ High-Resolution NMR in Microfluidic Devices. *262*, 73–80.

(14) Sharma, M.; Utz, M. Modular Transmission Line Probes for Microfluidic Nuclear Magnetic Resonance Spectroscopy and Imaging. *303*, 75–81.

(15) Patra, B.; Sharma, M.; Hale, W.; Utz, M. Time-Resolved Non-Invasive Metabolomic Monitoring of a Single Cancer Spheroid by Microfluidic NMR. *Sci. Rep.* **2021**, *11*, 53.

(16) Rogers, G.; Barker, S.; Sharma, M.; Khakoo, S.; Utz, M. Operando NMR Metabolomics of a Microfluidic Cell Culture. *J. Magn. Reson.* **2023**, *349:107405.*

(17) Jenne, A.; von der Ecken, S.; Moxley-Paquette, V.; Soong, R.; Swyer, I.; Bastawrous, M.; Busse, F.; Bermel, W.; Schmidig, D.; Kuehn, T.; Kuemmerle, R.; Al Adwan-Stojilkovic, D.; Graf, S.; Frei, T.; Monette, M.; Wheeler, A. R.; Simpson, A. J. Integrated Digital Microfluidics NMR Spectroscopy: A Key Step toward Automated In Vivo Metabolomics. *Anal. Chem.* **2023**, *95*, 5858–5866.

(18) Chen, J.; Tian, J.; Chen, Y.; Wu, T.; Sun, H.; Xie, J.; You, X.; Chen, Z. Probing the Kinetics of Chemical Reactions in Ultra-Small Droplet Samples Using Digital Microfluidic Nuclear Magnetic Resonance Spectroscopy. *Microchem. J.* **2023**, *193*, 108984.

(19) Eills, J.; Budker, D.; Cavagnero, S.; Chekmenev, E. Y.; Elliott, S. J.; Jannin, S.; Lesage, A.; Matysik, J.; Meersmann, T.; Prisner, T.; Reimer, J. A.; Yang, H.; Koptyug, I. V. Spin Hyperpolarization in Modern Magnetic Resonance. *123*, 1417–1551.

(20) Vaeggemose, M.; F. Schulte, R.; Laustsen, C. Comprehensive Literature Review of Hyperpolarized Carbon-13 MRI: The Road to Clinical Application. *11*, 219.

(21) Woitek, R.; Gallagher, F. A. The Use of Hyperpolarised 13C-MRI in Clinical Body Imaging to Probe Cancer Metabolism. *124*, 1187–1198.

(22) Park, S.; Rintaro, H.; Kim, S. K.; Park, I. Characterization of Distinctive In Vivo Metabolism between Enhancing and Non-Enhancing Gliomas Using Hyperpolarized Carbon-13 MRI. *Metabolites* **2021**, *11*, 504.

(23) Park, I.; Kim, S.; Pucciarelli, D.; Song, J.; Choi, J. M.; Lee, K.-H.; Kim, Y. H.; Jung, S.;

Yoon, W.; Nakamura, J. L. Differentiating Radiation Necrosis from Brain Tumor Using Hyperpolarized Carbon-13 MR Metabolic Imaging. *Mol. Imaging Biol.* **2021**, *23*, 417–426.

(24) Perkons, N. R.; Johnson, O.; Pilla, G.; Profka, E.; Mercadante, M.; Ackerman, D.; Gade, T. P. F. Functional Genetic Screening Enables Theranostic Molecular Imaging in Cancer. *Clin. Cancer Res.* **2020**, *26*, 4581–4589.

(25) Perkons, N. R.; Johnson, O.; Pilla, G.; Gade, T. P. F. Pharmacodynamics and Pharmacokinetics of Hyperpolarized [1−^{13}C]-Pyruvate in a Translational Oncologic Model. *NMR Biomed.* **2021**, *34*, e4502.

(26) Martinho, R. P.; Bao, Q.; Markovic, S.; Preise, D.; Sasson, K.; Agemy, L.; Scherz, A.; Frydman, L. Identification of Variable stages in Murine Pancreatic Tumors by a Multiparametric Approach Employing Hyperpolarized ^{13}C MRSI, ^{1}H Diffusivity and ^{1}H T_1 MRI. *NMR Biomed.* **2021**, *34*, e4446.

(27) Woitek, R.; McLean, M. A.; Gill, A. B.; Grist, J. T.; Provenzano, E.; Patterson, A. J.; Ursprung, S.; Torheim, T.; Zaccagna, F.; Locke, M.; Laurent, M.-C.; Hilborne, S.; Frary, A.; Beer, L.; Rundo, L.; Patterson, I.; Slough, R.; Kane, J.; Biggs, H.; Harrison, E.; Lanz, T.; Basu, B.; Baird, R.; Sala, E.; Graves, M. J.; Gilbert, F. J.; Abraham, J. E.; Caldas, C.; Brindle, K. M.; Gallagher, F. A. Hyperpolarized ^{13}C MRI of Tumor Metabolism Demonstrates Early Metabolic Response to Neoadjuvant Chemotherapy in Breast Cancer. *Radiol. Imaging Cancer* **2020**, *2*, e200017.

(28) Woitek, R.; McLean, M. A.; Ursprung, S.; Rueda, O. M.; Garcia, R. M.; Locke, M. J.; Beer, L.; Baxter, G.; Rundo, L.; Provenzano, E.; Kaggie, J.; Patterson, A.; Frary, A.; Field-Rayner, J.; Papalouka, V.; Kane, J.; Benjamin, A. J. V.; Gill, A. B.; Priest, A. N.; Lewis, D. Y.; Russell, R.; Grimmer, A.; White, B.; Latimer-Bowman, B.; Patterson, I.; Schiller, A.; Carmo, B.; Slough, R.; Lanz, T.; Wason, J.; Schulte, R. F.; Chin, S.-F.; Graves, M. J.; Gilbert, F. J.; Abraham, J. E.; Caldas, C.; Brindle, K. M.; Sala, E.; Gallagher, F. A. Hy-

perpolarized Carbon-13 MRI for Early Response Assessment of Neoadjuvant Chemotherapy in Breast Cancer Patients. *Cancer Res.* **2021**, *81*, 6004–6017.

(29) Ardenkjær-Larsen, J. H.; Fridlund, B.; Gram, A.; Hansson, G.; Hansson, L.; Lerche, M. H.; Servin, R.; Thaning, M.; Golman, K. Increase in Signal-to-Noise Ratio of >10,000 Times in Liquid-State NMR. *100*, 10158–10163.

(30) Kurhanewicz, J.; Vigneron, D. B.; Ardenkjaer-Larsen, J. H.; Bankson, J. A.; Brindle, K.; Cunningham, C. H.; Gallagher, F. A.; Keshari, K. R.; Kjaer, A.; Laustsen, C.; Mankoff, D. A.; Merritt, M. E.; Nelson, S. J.; Pauly, J. M.; Lee, P.; Ronen, S.; Tyler, D. J.; Rajan, S. S.; Spielman, D. M.; Wald, L.; Zhang, X.; Malloy, C. R.; Rizi, R. Hyperpolarized 13C MRI: Path to Clinical Translation in Oncology. *21*, 1–16.

(31) Hövener, J.-B.; Pravdivtsev, A. N.; Kidd, B.; Bowers, C. R.; Glöggler, S.; Kovtunov, K. V.; Plaumann, M.; Katz-Brull, R.; Buckenmaier, K.; Jerschow, A.; Reineri, F.; Theis, T.; Shchepin, R. V.; Wagner, S.; Bhattacharya, P.; Zacharias, N. M.; Chekmenev, E. Y. Parahydrogen-Based Hyperpolarization for Biomedicine. *57*, 11140–11162.

(32) Nagel, L.; Gierse, M.; Gottwald, W.; Ahmadova, Z.; Grashei, M.; Wolff, P.; Josten, F.; Karaali, S.; Müller, C. A.; Lucas, S.; Scheuer, J.; Müller, C.; Blanchard, J.; Topping, G. J.; Wendlinger, A.; Setzer, N.; Sühnel, S.; Handwerker, J.; Vassiliou, C.; van Heijster Frits H.A.; Knecht, S.; Keim, M.; Schilling, F.; Schwartz, I. Parahydrogen-Polarized [1-13C]Pyruvate for Reliable and Fast Preclinical Metabolic Magnetic Resonance Imaging. *10*, 2303441.

(33) Eills, J.; Hale, W.; Utz, M. Synergies Between Hyperpolarized NMR and Microfluidics: A Review. *Prog. Nucl. Magn. Reson. Spectrosc.* **2022**, *128*, 44–69.

(34) Bowers, C. R.; Weitekamp, D. P. Parahydrogen and Synthesis Allow Dramatically Enhanced Nuclear Alignment. *J. Am. Chem. Soc.* **1987**, *109*, 5541–5542.

(35) Duckett, S. B.; Sleigh, C. J. Applications of the Parahydrogen Phenomenon: A Chemical Perspective. *Prog. Nucl. Magn. Reson. Spectrosc.* **1999**, *34*, 71–92.

(36) Reineri, F.; Cavallari, E.; Carrera, C.; Aime, S. Hydrogenative-PHIP Polarized Metabolites for Biological Studies. *MAGMA* **2021**, *34*, 25–47.

(37) Eills, J.; Hale, W.; Sharma, M.; Rossetto, M.; Levitt, M. H.; Utz, M. High-Resolution Nuclear Magnetic Resonance Spectroscopy with Picomole Sensitivity by Hyperpolarization on a Chip. *J. Am. Chem. Soc.* **2019**, *141*, 9955–9963.

(38) Barker, S. J.; Dagys, L.; Hale, W.; Ripka, B.; Eills, J.; Sharma, M.; Levitt, M. H.; Utz, M. Direct Production of a Hyperpolarized Metabolite on a Microfluidic Chip. *Anal. Chem.* **2022**, *94*, 3260–3267.

(39) Ostrowska, S. J.; Rana, A.; Utz, M. Spatially Resolved Kinetic Model of Parahydrogen Induced Polarisation (PHIP) in a Microfluidic Chip. *ChemPhysChem* **2021**, *22*, 2004–2013.

(40) Sharma, M.; Utz, M. Modular Transmission Line Probes for Microfluidic Nuclear Magnetic Resonance Spectroscopy and Imaging. *J. Magn. Reson.* **2019**, *303*, 75–81.

(41) Stevanato, G.; Eills, J.; Bengs, C.; Pileio, G. A Pulse Sequence for Singlet to Heteronuclear Magnetization Transfer: S2hM. *J. Magn. Reson.* **2017**, *277*, 169–178.

(42) Eills, J.; Hale, W.; Sharma, M.; Rossetto, M.; Levitt, M. H.; Utz, M. High-Resolution Nuclear Magnetic Resonance Spectroscopy with Picomole Sensitivity by Hyperpolarization on a Chip. *J. Am. Chem. Soc.* **2019**, *141*, 9955–9963.

(43) Ripka, B.; Eills, J.; Kouřilová, H.; Leutzsch, M.; Levitt, M. H.; Münnemann, K. Hyperpolarized Fumarate *via* Parahydrogen. *Chem. Commun.* **2018**, *54*, 12246–12249.

(44) Stewart, N. J.; Nakano, H.; Sugai, S.; Tomohiro, M.; Kase, Y.; Uchio, Y.; Yamaguchi, T.; Matsuo, Y.; Naganuma, T.; Takeda, N.; Nishimura, I.; Hirata, H.; Hashimoto, T.; Matsumoto, S. Hyperpolarized ^{13}C Magnetic Resonance Imaging of Fumarate Metabolism by Parahydrogen-induced Polarization: A Proof-of-Concept *in vivo* Study. *ChemPhysChem* **2021**, *22*, 915–923.

(45) Knecht, S.; Blanchard, J. W.; Barskiy, D.; Cavallari, E.; Dagys, L.; Van Dyke, E.; Tsukanov, M.; Bliemel, B.; Münnemann, K.; Aime, S.; Reineri, F.; Levitt, M. H.; Buntkowsky, G.; Pines, A.; Blümler, P.; Budker, D.; Eills, J. Rapid Hyperpolarization and Purification of the Metabolite fumarate in Aqueous Solution. *Proc. Natl. Acad. Sci. U.S.A.* **2021**, *118*, e2025383118.

(46) Eills, J.; Cavallari, E.; Carrera, C.; Budker, D.; Aime, S.; Reineri, F. Real-Time Nuclear Magnetic Resonance Detection of Fumarase Activity Using Parahydrogen-Hyperpolarized [1-^{13}CC]Fumarate. *J. Am. Chem. Soc.* **2019**, *141*, 20209–20214.

(47) Wienands, L.; Theiß, F.; Eills, J.; Rösler, L.; Knecht, S.; Buntkowsky, G. Optimizing the Reaction Conditions for the Formation of Fumarate via Trans-Hydrogenation. *Appl. Magn. Reson.* **2022**, *53*, 615–634.

(48) Kating, P.; Wandelt, A.; Selke, R.; Bargon, J. Nuclear Singlet/Triplet Mixing During Hydrogenations with Parahydrogen: an in situ NMR Method to Investigate Catalytic Reaction Mechanisms and Their Kinetics. 2. Homogeneous Hydrogenation of 1,4-dihydro-1,4-epoxynaphthalene Using Different Rhodium Catalysts. *J. Phys. Chem.* **1993**, *97*, 13313–13317.

(49) Markelov, D. A.; Kozinenko, V. P.; Knecht, S.; Kiryutin, A. S.; Yurkovskaya, A. V.; Ivanov, K. L. Singlet to Triplet Conversion in Molecular Hydrogen and its Role in Parahydrogen Induced Polarization. *Phys. Chem. Chem. Phys.* **2021**, *23*, 20936–20944.

(50) Bargon, J.; Kandels, J.; Kating, P. Nuclear Magnetic Resonance Studies of Homogeneous Catalysis Using Parahydrogen: Analysis of Nuclear Singlet–Triplet Mixing as a Diagnostic Tool to Characterize Intermediates. *J. Chem. Phys.* **1993**, *98*, 6150–6153.

(51) Dagys, L.; Bengs, C.; Levitt, M. H. Low-frequency Excitation of Singlet–Triplet Transitions. Application to Nuclear Hyperpolarization. *J. Chem. Phys.* **2021**, *155*, 154201.

(52) Ostrowska, S.; Dagys, L.; Utz, M.; Levitt, M. Raw Data for: Efficient Parahydrogen Induced 13C Hyperpolarization on a Microfluidic Device. https://zenodo.org/records/11108345.